An Evolving Model of Surface Profile Produced by Nanosecond laser Ablation on Aluminum Alloy

Yang-zhi Chen, Xiong-dun Xie and Xiao-ping Xiao

School of Mechanical and Automotive Engineering, South China University of Technology, 381 Wushan Rd, Tianhe, Guangzhou 510640, China
E-mail: meyzchen@scut.edu.cn

Nanosecond pulse laser ablation (NSPLA) of solid is potential in micromachining. In order to provide a theoretical basis for the application of nanosecond laser ablation in high precision machining of three-dimensional structures, this paper studies the formation process of micro craters produced by NSPLA on aluminum alloy workpiece. The model uses an evolution method to calculate the ablation morphology which means the thermal process is calculated step by step and the ablation surface changes at each time step until it tends to the final morphology. The calculate processes are as follows: Firstly, the temperature distribution of target material subject to laser radiation is considered. Secondly, material removal based on normal evaporation and phase explosion are considered. Lastly, the evolution of the ablation surface during and after a nanosecond laser pulse is presented. The model predicts the geometry of the micro craters produced by nanosecond pulse laser of different power density, and the average depth of the grooves developed by different scanning speed of laser beam. A set of experiments were carried out that proved the practicability of the model. The present model and methods are meaningful to application of NSPLA into precision machining of microstructure and micro mechanical components.

DOI: 10.2961/jlmn.2019.02.0007

Keywords: nanosecond pulse laser, micro ablated crater, surface profile, heat conduction, evolving model

1 Introduction

Since 1980s, pulsed laser ablation (PLA) of solids has been applied to micro manufacture[1], pulse laser deposition of thin films (PLD)[2], nanoparticle formation[3] and nanofiber fabrication[4], etc. The micro manufacture technology selected for precise machining micro components with size range 10-1000μm should consider machining efficiency, precision and economic factor. Picosecond pulse laser ablation (PSPLA) and femtosecond pulse laser ablation (FSPLA) achieve extremely high machining precision, but have low material removal rate and require costly equipment, so they are more suitable for micro structure or parts with size about or beneath 10μm. Nanosecond pulse laser ablation (NSPLA), however, have a comprehensive advantage of efficiency, accuracy and economic factors in manufacturing micro parts with size range 10-1000μm. For choosing optimal machining parameters in manufacture processes, it is vital to have a deep understanding of material removal mechanism of NSPLA and model the machining process of NSPLA of metal workpiece.

For metal and metal-like materials exposed to nanosecond laser pulses, the two main mechanisms of material removal are normal evaporation and phase explosion[5]. Zhang Y[6], Gusarov A V[7], Lutey A H A[8], Gragossian A[9] build material removal models based on these mechanisms. Normal boiling, which occurs due to heterogeneous nucleation, does not prevail for ns pulses. This is because it involves a time scale of several micro seconds that is substantially higher than the pulse duration of ns[10]. These mechanisms are in thermal form because the pulse duration is greater than the electron relaxation time. The metal target material is experiencing all the following processes: electron excitation, energy transition between electron and lattice, phase change and diffusive flow of material, surface relaxation and recombination, and establish a thermodynamic equilibrium during the pulse[5].

Some studies were presented focusing on the relation between the laser parameters and the material removal efficiency, ablation threshold of the target material, depth and diameter of the craters[11][12][13]. These are helpful to select optimal parameters for different processing purposes.

Micro craters are formed during the interaction of high energy nanosecond pulse laser beam and target material. These craters are the smallest units of material removal in nanosecond pulsed laser processing of three-dimensional structures. As a result, the features of the crater, including the depth, diameter and geometry shape are of great importance in micro manufacture [1]. Some researchers focused on the ablation surface and geometry shape of the craters depending on laser parameters. For example, Bordatchev E V[14] carried out statistical analysis to search for patterns of technological parameters and crater features.

The features of the craters are closely related to the evolution process of ablation. Some researchers focus on the forming process of ablation surface, for example，Zhang W[15], etc used numerical methods to calculate the micro ablation surface of copper target material under consideration of Steffen conditions and discontinuity in Knudsen layer; Vatsya S R[16][17], etc presented a model describing the change of geometrical of surface profile under pulse

laser energy input. Generally, the attention is given to the depth and width of ablative craters.

This paper studies the evolution process of micro ablation surface of metal in NSPLA. It is more flexible and simpler to predict the geometry of the craters compared with existence models. When the shape and width of nanosecond pulse change, the corresponding ablation morphology can be obtained more conveniently, because the ablation morphology at any time after the laser pulse is applied to the target surface can be obtained during the calculation of the evolution process.

The target materials of 6061 aluminum alloy was selected as example in experimental verification. The experiments proved the practicability of the model to predict the depth, diameter and geometry shape of the craters. Also, the model shows good predictive ability on the average depth of straight grooves generated by overlapping of craters. The study is meaningful to application of NSPLA into micro structure manufacture and high efficiency and precision machining of micro machinery parts.

2 Mathematical model

The model presented in this paper predicts the micro craters' geometry shape by calculating of the evolution process of the ablation surface during and after a nanosecond laser pulse. Specifically, the model adopts iterative calculation method: Ablation time is subdivided into short periods of time as time steps. At the beginning of every period, the former ablation surface is subdivided into a set of points, whose ablation velocity vectors are calculated. The product of the velocity vector of each point and the time period length gives the respective displacement vector, and each point moves to a new point. Finally, a new ablation surface at the end of a time period is formed by a series of new points. The changes of the new surface compared with the old surface show the evolution process of the morphology during the formation of a micro-ablation crater. The cycle iterative calculation is carried out according to the set time step until the end of the ablation process, and the final ablation micro craters' geometry shape is obtained.

In the above model establishment, the magnitude of velocity vectors of the points at different positions on the ablation surface is equal to the surface recession velocity of the target, that is the sum of material removal rates of normal evaporation and phase explosion in the assumptions; The directions of velocity vectors are the normal directions of the ablation surface at different positions of the target.

In section 2, mathematical model has four parts in order of derivation: The section 2.1 presents for laser power input by giving of the spatial and temporal intensity distribution of pulsed laser energy on target surface, which acts as external input energy term in the heat conduction calculation. In section 2.2, based on 2D heat conduction equation, the temperature distribution of target slab before its surface reaches boiling point is calculated, that is the heating process before significant material removal. The temperature distribution is taken as an initial condition of section 2.3; In section 2.3, the material removal rate V_{ev} and V_{ex}, which are caused by normal evaporation and phase explosion respectively, are derived from heat transfer process of target slab beyond boiling point under moving boundary condition. Because the laser energy is partially shielded by the removed material, the shielding effect is considered and the calculation of laser energy is modified; Finally, in section 2.4**,** according to the calculation of material removal rate in section 2.3, a model calculating the surface morphology evolution process of ablation craters is established and micro craters' geometry shape of 6061 aluminum alloy target laser micro-ablation is obtained by iterative calculation.

Table 1 Parameters of 6061 Al aluminum

Parameters	sym-	unit	value
Room temperature	T_0	K	298.5
Melting point	T_m	K	933
Boiling point	T_b	K	2703
Critical point	T_c	K	8860
Evaporation latent heat	L_v	J/kg	1.05×10^7
Melting latent heat	L_m	J/kg	3.98×10^5
Specific heat(solid)	C_s	J/kgK	1050
Specific heat(liquid)	C_l	J/kgK	921
Density(solid)	ρ_s	kg/m^3	2549
Density(liquid)	ρ_l	kg/m^3	2224
Density (T_c)	ρ_c	kg/m^3	280
Thermal conduction (solid)	K_s	W/mK	223
Thermal conduction (liquid)	K_l	W/mK	106
Reflectivity(solid)	R_s	1	0.92
Reflectivity(liquid)	R_l	1	0.80
absorption coefficient	α_b	m^{-1}	1.21×10^8

2.1 laser power input

The pulse laser has a wavelength of 1064nm. Eq. (1) is used to describes a Q-switched pulse laser intensity distribution on the surface of the workpiece. n is related to the energy concentration. Q-switched fiber laser is used in this paper and $n=2$ best fit the performance testing result of the laser devise.

$$I(t,r)=\begin{cases} I_{pk}\left(\dfrac{t}{t_{\max}}\right)^n \exp\left(n\left(1-\dfrac{t}{t_{\max}}\right)\right)\exp\left(-\dfrac{r^2}{2\omega^2}\right), 0\le t\le\tau \\ 0 \qquad\qquad\qquad\qquad\qquad\qquad\qquad\qquad , \quad t>\tau \end{cases} \tag{1}$$

$$I_{pk}=\frac{\alpha_0\dfrac{Q_{\max}}{\pi\omega^2}}{\displaystyle\int_0^{\tau}\left(\frac{t}{t_{\max}}\right)^n\exp\left(n\left(1-\frac{t}{t_{\max}}\right)\right)dt} \tag{2}$$

In Eqs. (1)-(2), I_{pk} denotes the peak power of the pulse laser; $t_{\max}$ is the time when a pulse reaches its peak. From the performance testing result of the laser devise,

$t_{\max}=30$ns ;

spot radius $\omega=10$μm ;

pulse duration $\tau=100$ns ;

pulse energy $Q_{\max} = 0.8\text{mJ}$;

power percentage $\alpha_0 = 5\% - 100\%$

In the case of $\alpha_0 = 100\%$, the laser beam has a peak power of $I_{pk} = 4.78\text{GW/cm}^2$.

2.2 Heating of target material

The target workpiece undergoes a heating process under the radiation of laser. Ignoring the heat conduction of air, thermal radiation, convective heat transfer of molten material and Latent heat of melting, the axisymmetric heat process is governed by Eq. (3). Before material removal occurs, all boundaries of the governing equation are fixed. Then, the time when different locations on target slab surface reach melting and boiling temperature can be calculated. Based on the result, the size of the craters produced by pulse laser with different power density is roughly estimated. Most importantly, the starting time of surface recession is calculated

$$\begin{cases} C\rho\dfrac{\partial T(x,r,t)}{\partial t} - K\left(\dfrac{\partial^2 T(x,r,t)}{\partial x^2} + \dfrac{\partial^2 T(x,r,t)}{\partial r^2} + \dfrac{1}{r}\dfrac{\partial T(x,r,t)}{\partial r}\right) = (1-R)\alpha_b I(t,r)\exp(-\alpha_b x), \quad (0<r<\infty, 0<x<d, T<T_b) \\ -K\dfrac{\partial T(x,r,t)}{\partial x}\Big|_{x=0} = (1-R)\alpha_b I(t,r) \\ T(x,r,t)\big|_{x=d} = T_0 \\ T(x,r,t)\big|_{r=0} < \infty \\ T(x,r,t)\big|_{t=0} = T_0 \end{cases} \tag{3}$$

In Eq.(3), x denotes the direction perpendicular to the surface of the target, that is, the direction of target thickness; r denotes the horizontal direction, namely the direction of the spot radius. The parameters of target material are listed in Table 1, which are used throughout the whole paper. The value of C , ρ , K and R depend on the physical state of the material. d is the thickness of the slab, $d = 5\text{mm}$.

The calculation ends when the surface temperature reaches the boiling temperature T_b . Fig. 1 shows the time reaching melting and boiling temperature on the surface of the slab with different laser fluence and distance to the spot center. p40%， p60%, and p100% represent different values of α_0 which lead to various laser fluence correspondingly. The expression is used throughout the following paper. Under p100% power density, at the center of the laser spot, it takes 4.4ns and 7.8ns to reach the melting and boiling temperature respectively. The melting and boiling time are lengthened with decreasing of laser fluence and increasing of distance to the center of the laser spots.

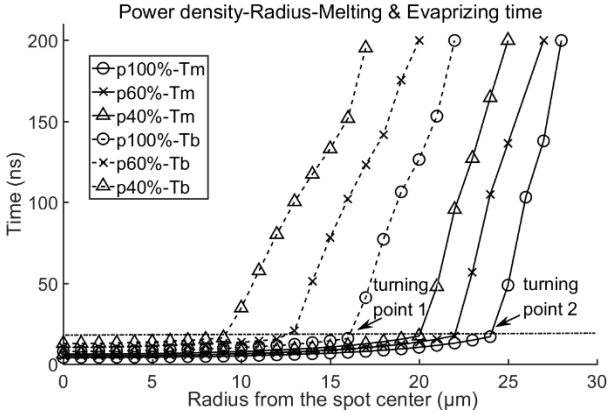

Fig. 1 Starting time of melting and evaporating -radius from laser spot center.

The size of the ablated craters can be roughly estimated, including the area of material removal and the molten pool. As can be seen in Fig. 1, there are some sudden turns in these curves which represents the melting or evaporating affected zone. For example, two turning points are marked in Fig. 1, turning point 1 suggests that under p100% power density, the evaporating zone with obvious material removal is a circular region with radius of 16μm, and turning point 2 suggests that in p100% power density, the melting affected zone is a circular region with a radius of 24μm. Other turning points have similar meanings.

2.3 Target material removal

In this section, surface recession velocities caused by normal evaporation and phase explosion, namely V_{ev} and V_{ex} are derived which represent material removal volume per unit area per unit time. Before calculating the temperature distribution, the shielding effect should be considered to correct the laser energy input.

When material removal begins, an expanding plume of vapor and liquid, reflect and absorb part of laser energy [8]. The laser distribution on the slab surface is reduced from $I(t,r)$ given in Eq. (1) to $I_{sh}(t,r)$ given in Eq. (4).

$$I_{sh}(t,r) = I(t,r)\exp(-\alpha_a(t)d_a(t)) \tag{4}$$

In Eq. (4)， $\alpha_a(t)$ denotes the actual absorption rate of the expanding plume and $d_a(t)$ denotes the depth of the expanding plume. They vary with time during the ablation process. The plasma energy absorption of laser by means of inverse bremsstrahlung (IB) and photo-ionization (PI) can be calculated [6][18], and the dimensions of the expanding plume can be calculated by gas dynamics equation [6].

In this paper, the shielding effect is calculated by a simulated method adopted in Ref [8] and Ref [19], that refers to the estimation of plasma shielding proposed by Singh and Viatella [21]. It assumes that the geometry of the expanding plume is as linear and its density as proportional to the ablation depth at any fixed point in time. The approximate calculation of shielding effect [8] [19] is given in Eq. (5).

$$\alpha_a(t)d_a(t) = \alpha_{sh}\Delta Z_{pe}(t) \tag{5}$$

In Eq. (5), $\Delta Z_{pe}(t)$ is the phase explosion depth of the target without considering shielding effect, which is estimated by $\Delta Z_{pe}(t)=\int_0^{\tau} v(t)dt$. Where, $v(t)$ is the recession velocity of the ablation surface， given in Eq. (6), which is derived by heat conduction equation under one-dimension motion boundary condition.

$$v(t)=\frac{I(t,0)}{\left(L_v\rho_l+C_l\rho_l(-T_m+T_b)\left(1+\frac{-T_0+T_m+\frac{L_m}{C_l}}{-T_m+T_b}\right)\right)} \tag{6}$$

In Eq. (5), α_{sh} is the simulated shielding coefficient [8] [19], obtained according to the following method: α_{sh} acts as the fitting parameters, and it's fitting criteria is the minimization of standard deviation between the computational ablation depth $\Delta Z_{pe}(\tau)exp(-\alpha_{sh}\Delta Z_{pe}(\tau))$ and the data of experimental ablation depth H.

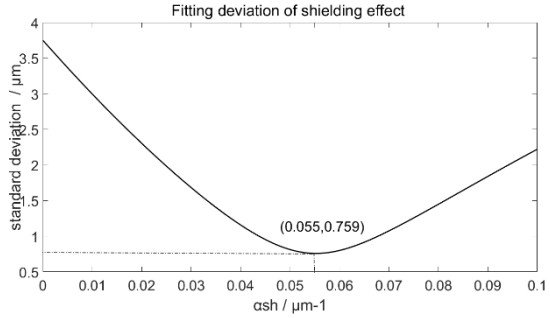

Fig. 2 Fitting deviation of shielding effect

According to the laser parameters and target material parameters adopted in this paper, it's fitting standard deviation calculated varies with α_{sh} which is shown in Fig. 2. It shows that minimum standard deviation is equal to $0.759\mu m$ at $\alpha_{sh}=0.055\mu m^{-1}$, which means the optimal value of simulated shielding coefficient in the example of this paper.

The above method is based on the collected experimental data and correction of fitting equation coefficients. After matching the fitting equation with experimental data, the optimal value of the parameters in the fitting equation is obtained, so that the fitting value is very close to the experimental results[20]. In terms of the fitting calculation of shielding effect, in a given working condition, including laser, target material and external environment parameters, the optimal α_{sh} is obtained by matching the experimental ablation depth data with the fitting equation of the model. The method allows estimation of laser shielding by the ablation products and ablation processing parameters without detailed knowledge of the plume dynamics.[19]. When working condition changes, α_{sh} needs to be recalibrated. For example, α_{sh} varies with the laser wavelength.[21].

After the laser energy input is corrected, the temperature distribution in material removal process is derived. Since the material has begun to be removed, the upper boundary of the governing equation is a moving boundary. The governing equation and its boundary conditions Eq. (7) [7] are used here. The initial temperature distribution is provided by section 2.2 when different points on surface temperature of the workpiece reach boiling temperature.

$$\begin{cases} C_l\rho_l(T)\dfrac{\partial T(x,t)}{\partial t}-C_l\rho_l(T)(V_{ev}(T)+V_{ex}(T))\dfrac{\partial T(x,t)}{\partial x}=\dfrac{\partial}{\partial x}\left(K(T)\dfrac{\partial T(x,t)}{\partial x}\right)+(1-R_l)\alpha_b I_{sh}(t,r)\exp(-\alpha_b x) \\ -K(T)\dfrac{\partial T(x,t)}{\partial x}\Big|_{x=0}=-L_v\rho_l(T)(V_{ev}(T_s)+V_{ex}(T(x)))+(1-R_l)I_{sh}(t,r) \\ T(x,t)\big|_{t=t_b}=T(x,t)_0\big|_{t=t_b} \end{cases} ,T>T_b \tag{7}$$

In Eq. (7), x denotes the direction perpendicular to the surface of the target slab. Since only the magnitude of material removal rate needs to be calculated, the governing equation is one-dimension and only the heat conduction perpendicular to the surface of the target is considered.

The heat conduction $K(T)$ and density of the material $\rho_l(T)$ [9][10] in Eq. (7) are given by Eqs. (8)-(9):

$$K(T)=-10^{-6}T^2-0.0048T+138.61, T>T_v \tag{8}$$

$$\rho_l(T)=\rho_c\left(1+0.75\left(1-\frac{T}{T_c}\right)+6.5\left(1-\frac{T}{T_c}\right)^{\frac{1}{3}}\right), T>T_m \tag{9}$$

Hertz-Knudsen Equation (10) gives the surface recession velocity due to normal evaporation V_{ev}, which varies with the surface temperature T_s. T_s is time-varying according to the calculation of Eq.(7).

$$V_{ev}(t)\approx\frac{0.82Mp_{sat}(T_s(t))}{\rho_l(T_s(t))\sqrt{2\pi k_B M T_s(t) N_A}} \tag{10}$$

$$p_{sat}(T_s)=p_{atm}\exp\left(\frac{L_v M}{k_B N_A}\left(\frac{1}{T_v}-\frac{1}{T_s}\right)\right) \tag{11}$$

In Eq.(10), M is the molar mass, k_B is the Boltzmann constant, N_A is the Avogadro's number. The sticking coefficient is taken as 1 and the back-flow coefficient as 0.82. The saturation pressure $p_{sat}(T_s)$ is given by the Clausius-Clapeyron Equations (11), where, T_v is equilibrium boiling temperature and p_{atm} is atmospheric pressure.

Normal evaporation occurs on the surface of the workpiece, while phase explosion occurs inside the superheated liquid. When the temperature of the superheated liquid is above $0.8T_c$, homogeneous nucleation is expected to occur, and the nucleation rate increases rapidly when the

temperature approaches $0.9T_c$ [6][9][19]. Phase explosion occurs when the bubbles reach critical radius and burst.

Miotello and Kelly[22] pointed out that explosive boiling may occur during the laser pulse. $V_{ex}(T(x))$, the material removal velocity caused by phase explosion, varies with the temperature spatial distribution along x direction at any fixed point in time. And the temperature spatial distribution is time-varying according to the calculation of Eq.(7). $V_{ex}(t)$ is given by Eq. (12).

$$V_{ex}(t)=\int_0^{h(F)} J(T(x,t))\frac{4\pi}{3}R_c(T(x,t))^3\frac{\rho_v(T(x,t))}{\rho_l(T(x,t))}dx \qquad (12)$$

In Eq. (12), $J(T)$ is the homogeneous nucleation rate in unit volume per unit time in superheated liquid, given in Eq.(13); $R_c(T)$, the critical radius of the bubble[23] is given in Eq.(16) ; $\frac{4\pi}{3}R_c(T)^3$ is the volume of a bubble. ρ_v denotes the density of gas which is given by Eq. (15).

$$J(T)=\frac{\rho_l}{m_a}\sqrt{\frac{3\gamma}{\pi m_a}}\exp(\frac{-\Delta G(T)}{k_BT}) \qquad (13)$$

In Eq. (13), γ denotes the surface tension of liquid; m_a denotes the mass of the particle; ΔG denotes the free energy for the formation of a stable homogeneous nucleus presented by Eq. (14)[7]; In Eq.(16), p_l is the pressure of the superheated liquid, which is estimated by $p_l=0.54p_{sat}(T)$ according to Ref [24].

$$\Delta G(T)=\frac{16\pi}{3}\gamma^2/\left(\rho_v L_v\left(\frac{T}{T_v}-1\right)\right)^2 \qquad (14)$$

$$\rho_v(T)=\frac{m_a}{k_BT}p_{atm}\exp\left(\left(\frac{T}{T_v}-1\right)m_aL_v/k_BT\right) \qquad (15)$$

$$R_c(T)=\frac{2\gamma}{p_{sat}(T)\exp\left(m_a\frac{p_l-p_{sat}(T)}{\rho_l k_BT}\right)-p_l} \qquad (16)$$

Table 2 Duration(ns) above $0.8T_c$ in different depth to the target surface

Power density J/cm^2	0.0 μm	0.2 μm	0.4 μm	0.6 μm	0.8 μm	1.0 μm	1.2 μm
254.6 (100%)	92.3	88.9	83.3	75.2	59.0	29.8	0
203.72 (80%)	86.8	83.0	76.5	61.3	36.6	0	0
152.79 (60%)	81.3	72.7	58.2	33.6	0	0	0
127.33 (50%)	71.9	61.3	42.6	0	0	0	0
101.86 (40%)	57.6	43.5	0	0	0	0	0
70.03(27.5%)	28.9	0	0	0	0	0	0

In Eq.(12), $h(F)$ is defined as the thickness of superheated liquid layer on where the temperature reaches or above $0.8T_c$ at which phase explosion starts to occur. $h(F)$ can be estimated according to the time that the materials at different depths stay over $0.8T_c$ under different power fluences. For example, $h=1\mu m$ under laser fluence of $254.65J/cm^2$, $h=0.8\mu m$ under laser fluence of $203.72J/cm^2$.The data of thickness of superheated liquid layer under different laser fluences are given in Table 2. The black squares indicate that the maximum depth at which $0.8T_c$ can be reached. $h(F)$ decreases as the laser fluence decreases. When the fluence is below $70J/cm^2$, it drops to zeros which means the phase explosion does not occur.

2.4 Evolving of surface profile

Normal evaporation and phase explosion occur according to $T(x,r,t)$. The expressions of V_{ev} and V_{ex} are obtained in section 2.3，which are used here to calculate the surface evolution process. According to Fig. 1 and calculation of Eq.(10), significant normal evaporation happens within the range of $r=0-25\mu m$ and $t=0-200ns$ .Phase explosion requires temperature of higher than $0.8T_c$ [6][9][19], so it also occur within these radius and time ranges.

The evolving model of the ablated surface profiles is presented in detail as follows:

The Computing ablation time range of $t=0\sim200ns$ is divided into 2000 time periods by a duration of $t_0=0.1ns$ for using an iterative method to calculate the change of surface profile. At the end of each time step, the thermal calculations of Eq.(7) are updated to account for changes in material properties and surface recession velocity of V_{ev} and V_{ex}. The Computing spatial range of $r=0\sim25\mu m$ is also divided into 250 separated points by an interval of $r_0=0.1\mu m$ for using a differential method. A set of separated points are calculated at the end of each time step representing the surface profile and then fitted by the form of Eq. (17), and served as the initial surface profile of the next time step. The bell shape function in Eq. (17) is chosen because it conforms well to the ablated surface in the experiments, where a and b are the shape parameters of the "bell".

$$z=\frac{a}{\sqrt{2\pi}}\exp(\frac{-br^2}{2a^2}) \qquad (17)$$

The evolution process is described as follows:

The target slab is half infinite with a flat surface at the first time step $i=0$, the coordinates of the interval points on the surface are $(R_{0,j},Z_{0,j})=(jr_0,0)$,so the surface profile at the first time step is $z_0=0$;

STEP 1 In the $(i)th$ time step, starting from $i=1$, the surface profile is moving along vertical direction from the former one. $z_{i-1}=z_{i-1}(r_{i-1})$ represents the former surface profile. The angle between the moving direction and the vertical direction at the $(j)th$ point with a radius of $R_{i,j}=(j-1)r_0$ are given by Eq. (18); And its coordinates are given by Eq. (19). In each time step, coordinates of 250 interval points are calculated by using Eqs. (18)-(19).

$$\begin{cases} \theta_{i,j} = 0, (i = 1) \\ \theta_{i,j} = \arctan\left(-\dfrac{dz_{i-1}}{dr_{i-1}}\right) = \arctan\left(-\dfrac{b_{i-1}R_{i-1,j}\exp(-\dfrac{b_{i-1}R_{i-1,j}^{\ 2}}{2a_{i-1}^{\ 2}})}{a_{i-1}\sqrt{2\pi}}\right) \\ , (i > 1) \end{cases}$$
$$(1 \le j \le 250, j \in Z) \qquad (18)$$

$$\begin{cases} R_{i,j} = R_{i-1,j} + \left(V_{ev}\left(T\left(it_0, jr_0\right)\right) + V_{ex}\left(T\left(it_0, jr_0\right)\right)\right)t_0 \sin\left(\theta_{i,j}\right) \\ Z_{i,j} = Z_{i-1,j} + \left(V_{ev}\left(T\left(it_0, jr_0\right)\right) + V_{ex}\left(T\left(it_0, jr_0\right)\right)\right)t_0 \cos\left(\theta_{i,j}\right) \end{cases},$$
$$(1 \le j \le 250, j \in Z) \qquad (19)$$

Fig. 3 demonstrates the evolution process in the $(i)th$ time step, solid line represents the ablation surface in $(i-1)th$ time step, which is divided into points in the radius direction. $P_1(R_{i-1,p1}, Z_{i-1,p1})$ and $P_2(R_{i-1,p2}, Z_{i-1,p2})$ are given as two examples here, in which $\theta_{i,p1}$ and $\theta_{i,p2}$ are the angles of displacement vectors, namely, the angle between normal of the surface and the vertical direction. The magnitudes of the displacement vectors for $P_{1(i-1)}$ and $P_{2(i-1)}$ are calculated by $V_{1\_i} = \left(V_{ev}\left(T\left(it_0, p_1r_0\right)\right) + V_{ex}\left(T\left(it_0, p_1r_0\right)\right)\right)t_0$ and $V_{2\_i} = \left(V_{ev}\left(T\left(it_0, p_2r_0\right)\right) + V_{ex}\left(T\left(it_0, p_2r_0\right)\right)\right)t_0$, respectively. Then, the coordinates of new points $P_1(R_{i,p1}, Z_{i,p1})$ and $P_2(R_{i,p2}, Z_{i,p2})$ after the evolution process of the $(i)th$ time step can be obtained by Eq. (18).

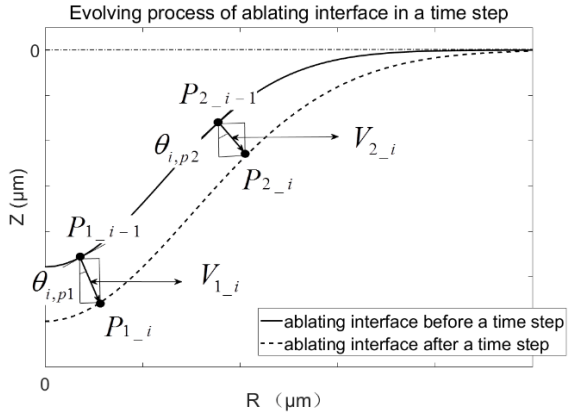

Fig. 3 Schematic diagram of the evolution process

STEP 2 The bell shape function Eq.(17) is applied to fit those 250 interval points $(R_{i,j}, Z_{i,j})$. A fitting curve $z_i = z_i(r_i)$ and its parameters a_i, b_i are obtained. As shown in Fig. 3, the dotted line is the new ablation surface.

STEP 3 The ablation surface profile $z_i = z_i(r_i)$ of the $(i)th$ time step is obtained, then $i = i+1$, the above processes are repeated until $i = 2000$, which means the final ablation surface is obtained. Fig. 4 demonstrates the results of the evolving model.

The shock wave in phase explosion causes intense movement, sputtering of the molten metal and displacement of material. That is why there are peaks at the edges and uneven bottom in the craters. The material displacement is random so that the craters in the experiments have differences in shape and depth. Fig. 5(a-d) shows the craters produced by laser pulses of different power. Red means high in altitude and blue means low in altitude.

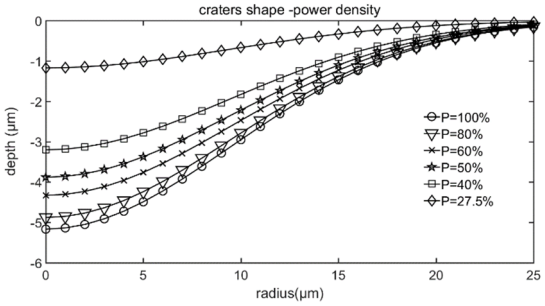

Fig. 4 Laser fluence – craters profiles

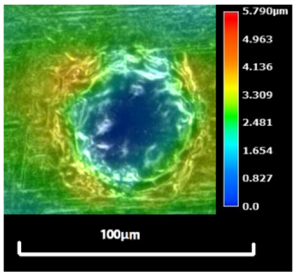

(a) crater (p100%)

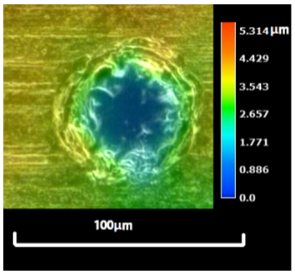

(b) crater (p80%)

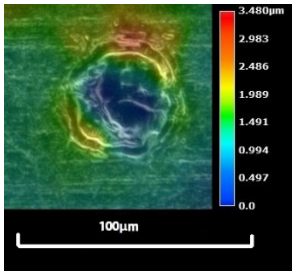

(c) crater (p60%)

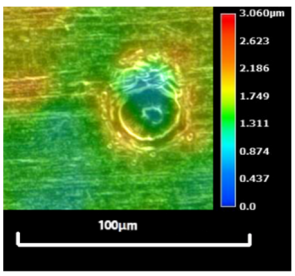

(d) crater (p40%)

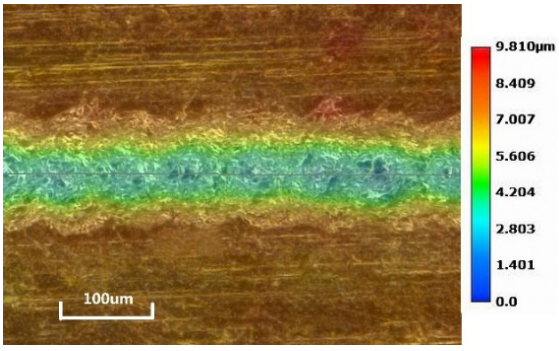

(e) straight groove (p80%, v1000mm/s)

Fig. 5 Ablation samples

3 Experiments

In this section, experiments are carried out to verify whether the model proposed conforms to the experimental results. Section 0 focuses on single craters' geometry shape

and Section 0 focuses on average depth and unevenness of straight grooves generated by overlapping craters, where overlap coefficient L is defined to represent the positional relation between the adjacent craters.

First, equipment in the experiments are listed as follows: The nanosecond pulse laser equipment used in this study is called a laser marking machine, by which the laser beam is generated by a Q-switched fiber laser with a wavelength of 1064nm and a pulse duration of 100ns whose brand is QSFl-20A made by Shenzhen super laser technology Co., Ltd, China. The transmitted beam is focused on the target surface by using of a set of lenses in brand of Carman Hass SL-1064-110-160, and the scanning galvanometer has a repeat accuracy of ± 100nm . The target metal slabs have a thickness of 5mm, which are cut off from a rolling plate into small pieces with surface roughness under 100nm . The target slab is irradiated normally in ambient air.

The geometry of each produced crater was characterized by using an optical ultra-depth of focus microscope (VHX-2000) with magnification times with a range of $100\times-1000\times$. Surface profile data can be read by a software which comes with the system then the height distribution data of different sections is exported to PC for further data processing.

3.1 Craters produced by single pulse ablation

A comparison of the geometry of craters calculated by the present model to the average experimental results produced by single pulse laser of different power density is shown in Fig. 6. There are 9 craters in each group. The red solid lines in each figure represent the calculating results, blue dash lines represent the average experimental results of 9 craters and three typical craters profile are given in each figure and the blue lines with markers are the typical craters in the experiments.

From the experimental results, the ablated depth matches well to the experiments under p100% and p80%, while the calculating craters are shallower under p60% and p40% respectively for the molten material movement. The molten pool is thicker under lower power density which means more sputtering material. The geometry error becomes bigger at larger radius area, because the material sputtering brings away some material to the edge of the craters.

The depth of the craters with error bars are shown in Fig. 7. "o" means the average depths of the produced craters; "*" means the calculating depth of the craters considering normal evaporation and phase explosion; "Δ" means the melting interface. As marked by the arrow in Fig. 8, the distance between the "*" line and "Δ" line represents the thickness of molten pool, it decreases slightly with the increase of power density, and the data are listed at the bottom of Fig. 7. And it is confirmed by Fig. 5(a-d) that as the laser power decreases, more sputtering liquid can be seen at the edge of the craters. It can be concluded that the model fits well with the data, in lower laser fluence, the molten pool has a greater impact on the carters' depth.

The presented results above are consistent to other researches of ablation removal model**[6][7][8][9]**, the increasing speed of the ablated depth decrease with the increasing power density, the relation is similar to logarithmic function.

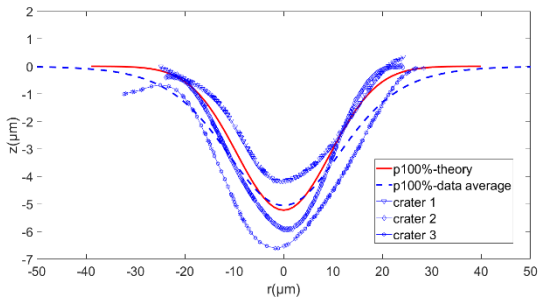

(a) p=100%

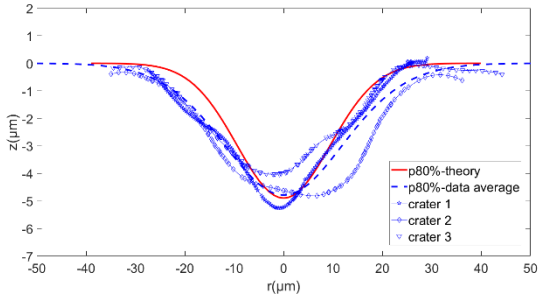

(b) p=80%

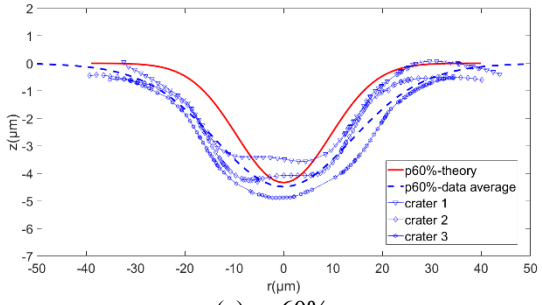

(c) p=60%

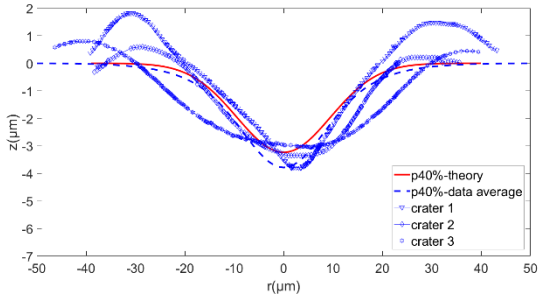

(d) p=40%

Fig. 6 Geometry of craters in model calculation and experimental results

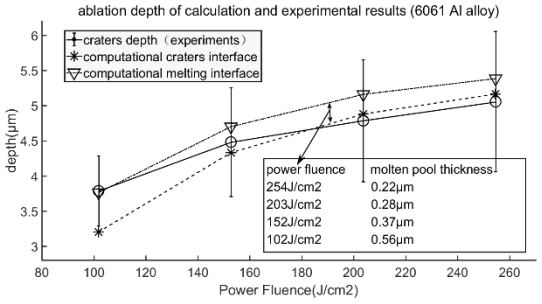

Fig. 7 Abating depth of different laser fluence

3.2 Straight grooves produced by overlapping of pulses

The scanning speed, filling model and scanning number of NSPLA affect the micro structure and surface profile of a

machined workpiece through changing the overlap of the craters. When pulse train is applied, there is a thermal accumulation effect. When the ambient temperature is 25°C, according to the calculating result by a two-dimension temperature diffusion model, each laser pulse brings a maximum temperature rise of 10°C on the target surface, In this example, pulse duration is 100 ns, The time interval is very short, at that pulse laser acts on the target surface to surface reaches boiling temperature, as shown in Fig. 1, no more than 10 ns. Increasing the initial temperature of 10° C will only make this time interval shorter, within the most error of 10 ns, having little effect on prediction of craters depth, within a few percent of the prediction deviation. In addition, this is the thermal accumulation generated by multiple impacts by repeated pulse at the same position and without concerning thermal radiation and air convection. In actual operating condition, the thermal accumulation has even less impact on the superposition of the ablation morphology. Therefore, the influence of thermal accumulation is ignored in the calculation of the ablation morphology here.

The size and surface roughness of the micro structure are key points, so the depth and surface unevenness at the bottom of the grooves are major concerns in this paper.

L , is defined as the overlap coefficient of the adjacent craters given by Eq.(20) . Where, D is the average diameter of the craters, c is the horizontal distance between the center points of two adjacent craters, referred to as center distance in the rest of this paper. According to the definition, $L \in (-\infty, 1]$.

$$L = \frac{D - c}{D} \tag{20}$$

In the case of $L \in (-\infty, 0)$, that is $c > D$,the craters are separated;

In the case of $L \in [0,1)$, that is $0 < c < D$, the craters are partly overlapped with each other;

In the case of $L = 1$, that is $c = 0$, the craters are completely overlapped that means repeated ablations happen at the same location.

p80% power density was selected in the experiments, while the scanning speed varies within the range of 600-2000mm/s, and the corresponding center distance of the craters is under a range of $[20.87\mu m, 62.61\mu m]$. The average diameter of the craters is D=50μm . According to Eq. (20), overlap coefficient $L \in [-0.39, 0.58]$.

Typical results of surface profile at the center cross section in the length direction of a straight groove are shown in Fig. 8, dash lines mean the computational results and solid lines mean the results measured by VHX-2000.

Fig. 9 demonstrates the average depth and unevenness at the bottom of the grooves varies with the overlapping. “o” line represents the computational average depth of grooves; “Δ” line represents average depth of grooves obtained in experiments; “*” line represents the computational unevenness at the bottoms of the grooves; “x” line represents the unevenness at the bottoms of the grooves obtained in experiments. The average depth matches well to the experiment results especially in case of high overlapping when L>0 . The bottom unevenness is calculated by standard deviation of the surface topography obtained in the experiments. Seen from Fig. 9, there is some deviation on estimation of unevenness. That is caused by the influences of spattering of the liquid metal are not considered in the calculations of this model.

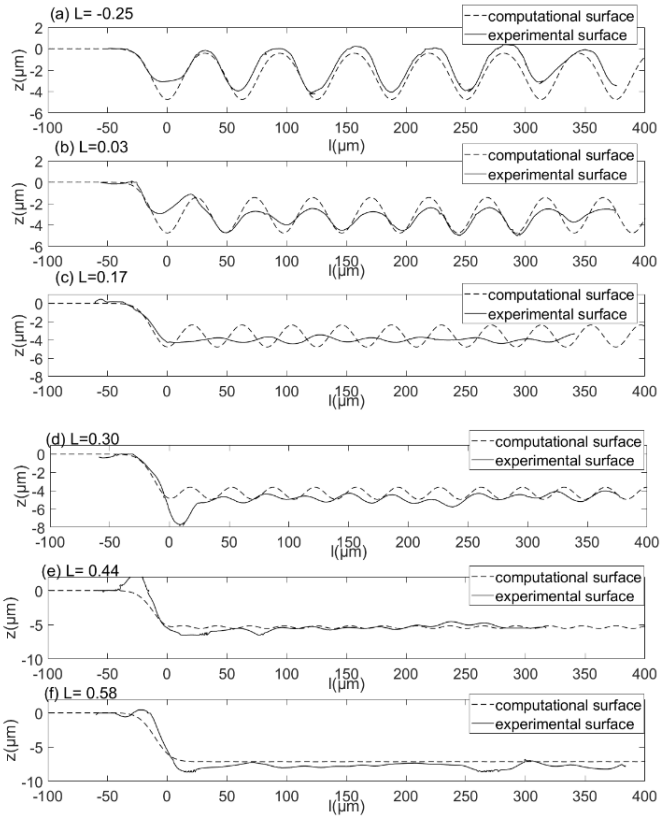

Fig. 8 Abating depth of different laser fluence grooves' profile in model calculation and experimental results

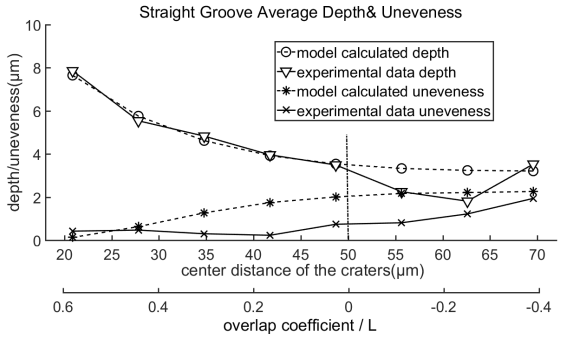

Fig. 9 Average depth and bottom unevenness of grooves

The spatter liquid has two characteristics, one is that under given laser power density and target material, the influence distance of the spatter liquid is basically fixed during the formation of each crater; The another is that the liquid spatters towards every direction is random, but the overall distribution is uniform when large number of craters are counted. This makes a basic conclusion, that separated craters shows their random morphologies and the random morphologies cancel out when the craters are overlapping. As shown in Fig. 5(a), the separated craters have deviation in shape, while the straight groove in Fig. 5(b) is more uniform at different positions.

In case of $L < -0.2$, the craters are away from each other,

As seen in Fig. 8(a), because the spatter liquid is deposited on the surface of the target between the craters, so the height of the experimental surface is higher than that of computational surface, even higher than the original zero-altitude surface at some peaks.

In case of $L \in (-0.2, 0.3]$, as shown in Fig. 8(b-c-d), the spatter liquid affects one to two nearest craters, and part of the material is deposited in the formed craters that reduces their depth. Also, part of the material deposited on the unablated target surface, which bulge the initial surface and thus reducing the depth of the next crater. As a result, the model overestimates the bottom unevenness of the grooves at this range.

In case of $L \in (0.3, 0.58]$, as shown in Fig. 8 (e-f), with an increasing of L, the spatter liquid affected area overlaps more. In this case, the splashes overlay each other, so the resulting unevenness trends to a fix range 0.2-0.5μm.

To be specified, the spatter only affects the distribution of materials and has little effect on the removal rate of materials. So, the model is accurate in estimating the average depth of the grooves.

4 Conclusions

Essentially, in NSPLA technology applied to micro structure or micro parts manufacture, the machining process is the superposition of minimum material removal units. Grooves, stairs, cones and other complicated 3D structure are produced by overlapping of micro craters. To meet the requirements of high efficiency and high precision in micro machining using NSPLA, the mechanisms of material removal and the formation process of surface profile need to be studied.

For this purpose, this paper has completed the following work:

1. An evolving model of surface profile produced by NSPLA is presented, that is on basis of normal evaporation and phase explosion.

2. 6061 aluminum alloy is selected as target material, the evolution of the ablation surface of target material under the radiation of nanosecond laser pulse is simulated in detail. The geometry of the craters produced by single laser pulse and that of grooves produced by overlapping of laser pulse are obtained.

3. A set of experiments were carried out in ambient air. The results show that the theoretical calculations of single ablation craters are in good agreement to the experimental results. Under different setting of laser beam scanning speed, the average depth of the grooves is consistence well with the that of model prediction.

In near future, the present model will be further studied and tested to verify the possibility of its applications to more metal materials. Furthermore, ablated profiles of multi-layer and different scanning patterns remain to be studied, which will provide better theoretical basis for NSPLA applying to complicated 3D structure.

Acknowledgments

This work was supported by National Natural Science Foundation of China (No. 51575191), the Fundamental Research Funds for the Central Universities (No.2017B0071, No. 2018PY12) and 2019 Guangzhou technology project (No201904010368).

References

[1] M.R.H. Knowles, G. Rutterford, D. Karnakis, and A. Ferguson: Int. J. Adv. Manuf. Tech., 33, (2007) 95.
[2] A.N. Zherikhin: Proc. Tenth International School on Quantum Electronics: Laser Physics & Applications. International Society for Optics and Photonics, (1999) p.72.
[3] Itina and E. Tatiana: J. Phys. Chem. C., 115, (2011) 5044.
[4] K. Venkatakrishnan, D. Vipparty and B. Tan: Opt. Express., 17, (2011) 19.
[5] M. Stafe, A. Marcu and N.N. Puscas: "Pulsed Laser Ablation of Solids" ed. by G. Ertl, H. Lüth and D.L. Mills, (Springer, Berlin Heidelberg, 2014) p.7.
[6] Y. Zhang, D. Zhang, J. Wu, et al: AIP Adv., 7, (2017) 075010.
[7] A.V. Gusarov, I. Smurov: J. Appl. Phys.,1, (2005) 291.
[8] A.H.A. Lutey: J. Appl. Phys., 8, (2013) 647.
[9] A. Gragossian, S.H. Tavassoli and B. Shokri: J. Appl. Phys., 10, (2009) 103.
[10] R. Kelly and A. Miotello: Appl. Phys., 6, (2000) 3177.
[11] B.B. Naghshine, A. Kiani, et al: AIP Adv., 2, (2017) 025007.
[12] N.M. Bulgakova and A.V. Bulgakov: Appl. Phys A., 2, (2001) 199.
[13] M.A. Jafarabadi and M.H. Mahdieh: Appl. Surf. Sci., 346 (2015) 263.
[14] E.V. Bordatchev and S.K. Nikumb: Mach. Sci. Technol., 1, (2003) 83.
[15] W. Zhang, Y.L. Yao and K. Chen: Int. J. Adv. Manuf. Tech., 5, (2001) 323.
[16] S.R. Vatsya, E.V. Bordatchev and S.K. Nikumb: J. Appl. Phys., 93, (2003) 9753.
[17] S.R. Vatsya, C. Li and S.K. Nikumb: J. Appl. Phys., 3, (2005) 91.
[18] D. Marla, U.V. Bhandarkar and S.S. Joshi: Appl. Phys. A., 1, (2014) 273.
[19] H.A. Adrian and Lutey. J. Manuf. Sci E., 135, (2013) 061003.
[20] H.G. Bock, T. Carraro, Willi Jäger, et al: "Model based parameter estimation" ed. by H.G. Bock, Willi Jäger and O. Venjakob, (Springer, Berlin Heidelberg, 2013) pp.1.
[21] R.K. Singh and J. Viatella: J. Appl. Phys., 2, (1994) 1204.
[22] A. Miotello and R.Kelly: Appl. Phys. Lett. 67, (1995) 3535.
[23] C. Porneala, D.A. Willis: Appl. Phys. Lett. 21, (2006) 3535.
[24] M.V. Allmen: "Laser-beam interactions with materials" (Springer, Verlag, 1987) p.146.

(Received: May 1, 2019, Accepted: August 25, 2019)